Effective nonlocal parity-dependent couplings in qubit chains

Maximilian Nägele [1,2] Christian Schweizer [1,2,3] Federico Roy [2,4] and Stefan Filipp [2,3,5]

[1]*Fakultät für Physik, Ludwig-Maximilians-Universität München, Schellingstraße 4, D-80799 München, Germany*
[2]*Walther-Meißner-Institut, Bayerische Akademie der Wissenschaften, 85748 Garching, Germany*
[3]*Munich Center for Quantum Science and Technology (MCQST), Schellingstraße 4, 80799 München, Germany*
[4]*Theoretical Physics, Saarland University, 66123 Saarbrücken, Germany*
[5]*Physik-Department, Technische Universität München, 85748 Garching, Germany*

(Received 3 May 2022; revised 21 July 2022; accepted 26 July 2022; published 30 August 2022)

For the efficient implementation of quantum algorithms, practical ways to generate many-body entanglement are a basic requirement. Specifically, coupling multiple qubit pairs at once can be advantageous and may provide multiqubit operations useful in the construction of hardware-tailored algorithms. Here we extend the theory of fractional state transfer and harness the simultaneous coupling of qubits on a chain to engineer a set of nonlocal parity-dependent quantum operations suitable for a wide range of applications. The resulting effective long-range couplings directly implement a parametrizable Trotter-step for Jordan-Wigner fermions, and they can be used for simulations of quantum dynamics, efficient state generation in variational quantum eigensolvers, parity measurements for error-correction schemes, and the generation of efficient multiqubit gates. Moreover, we present numerical simulations of the gate operation in a superconducting quantum circuit architecture, which show a high gate fidelity for realistic experimental parameters.

DOI: 10.1103/PhysRevResearch.4.033166

I. INTRODUCTION

In recent years, significant advances have been made in the field of quantum computing in demonstrating applications in which quantum devices are predicted to be advantageous [1–4]. A promising near-term application is the simulation of quantum-mechanical systems [5,6]. In particular, the simulation of fermionic systems is important to predict the properties of, e.g., molecules [7,8], or to understand many-body systems such as the Fermi-Hubbard model, which is expected to explain phenomena of great scientific and industrial interest such as high-temperature superconductivity [9]. However, mapping fermions to qubits poses a major challenge, since local fermionic couplings can result in nonlocal qubit interactions [10–12].

To build quantum processors, different physical platforms, such as trapped ions [13], superconducting qubits [14,15], quantum dots [16], neutral atoms [17], and photonic qubits [18], are currently considered. Independent of the platform, an important characteristic for each device's capability is the qubit connectivity, which is typically limited to local two-body couplings [19], while nonlocal interactions are challenging to implement and require a large amount of consecutive two-qubit gates [20] or auxiliary qubits [21,22].

An alternative solution is to implement nonlocal terms by controlling multiple two-body couplings simultaneously [23–28]. A prime example of such a method is the perfect state transfer along a qubit chain [29–37], where an excitation at an initial location is transferred to a final location along the chain. This technique has a large variety of applications, such as entanglement generation and effective two-qubit gates [38–42]. Recently, it has been extended to fractional state transfer (FST) [43–45], where the quantum state is partially transferred to the final location while the other part returns to its original position.

In this work, we build on FST and harness nearest-neighbor couplings in a linear chain of two-level systems to engineer effective nonlocal interactions that depend explicitly on the number of excitations in the chain (see Fig. 1). These interactions directly implement fermionic couplings between qubits on opposite sides of the chain under Jordan-Wigner transformation (JWT), and thus they generate a set of matchgates [46] that correspond to the unitary evolution of free fermions [47,48]. In addition to fermionic quantum simulation, the excitation-dependent operation also provides an efficient way to measure long strings of qubit correlators with potential applications in quantum error correction [49,50].

II. FRACTIONAL STATE TRANSFER

The Hamiltonian of a qubit chain with length N is given by

$$H_N = \sum_{n=1}^{N} \Delta_n \sigma_n^+ \sigma_n^- + \sum_{n=1}^{N-1} (J_n \sigma_n^+ \sigma_{n+1}^- + \text{H.c.}), \qquad (1)$$

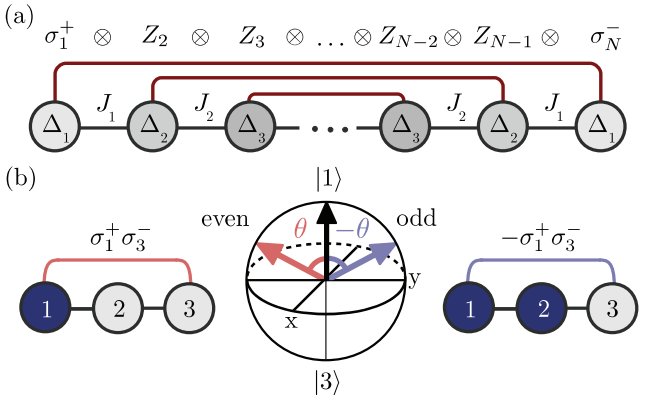

FIG. 1. Qubit chain and effective parity-dependent couplings. (a) Chain of qubits (circles) with frequencies Δ_n and direct couplings J_n, as described by H_N in Eq. (1). Dark red lines indicate effective nonlocal interactions that stroboscopically arise for specific parameter choices of Δ_n and J_n. The effective interaction results in a rotation in the subspaces spanned by $|n\rangle$ and $|N+1-n\rangle$, where n denotes the location of the excitation. The orientation of the rotation vector depends on the parity of the qubits between each pair, $\otimes_{k=n+1}^{N-n} Z_k$. (b) Illustration of a chain with length $N=3$. A single excitation is prepared at site 1 and partially transferred to site 3 with effective interaction $\sigma_1^+\sigma_3^- + \text{H.c.}$ (left chain), which rotates the state by an angle θ on the Bloch-sphere spanned by the states $|1\rangle$ and $|3\rangle$ (red arrow). If an additional excitation is prepared at site 2 (right chain), the effective interaction changes sign, so that the state is rotated by an angle $-\theta$ on the Bloch-sphere (blue arrow).

where we set $\hbar = 1$. Here, $\sigma_n^{\mp}$ are the qubit lowering (raising) operators and Δ_n is the frequency of qubit n. The coupling between qubits n and $n+1$ is mediated via XY-interactions $\sigma_n^+\sigma_{n+1}^- + \text{H.c.} = (X_nX_{n+1} + Y_nY_{n+1})/2$ with time-independent coupling strengths $J_n > 0$. We use the notation X, Y, Z, and I for the Pauli matrices and the identity.

To implement FST, we set $J_n = J_{N-n}$ and $\Delta_n = \Delta_{N+1-n}$ to be symmetric about the center. Since evolution under H_N preserves the total number of excitations in the system, each excitation manifold can be considered separately. Hence, we first consider FST in the single-excitation manifold, where H_N is tridiagonal and persymmetric, i.e., symmetric around its antidiagonal:

$$H_N^{(1)} = \begin{pmatrix} \Delta_1 & J_1 & & & \\ J_1 & \Delta_2 & J_2 & & \\ & \ddots & \ddots & \ddots & \\ & & J_2 & \Delta_2 & J_1 \\ & & & J_1 & \Delta_1 \end{pmatrix}. \tag{2}$$

As such, it has only mirror-symmetric and mirror-antisymmetric eigenvectors, $|v_j^s\rangle$ and $|v_j^a\rangle$, with real nondegenerate eigenvalues $\lambda_j^{s/a}$ [39,51]. Hence, we can expand the single-excitation basis state $|n\rangle = |0\cdots 1_n \cdots 0\rangle$ and its mirror state $|N+1-n\rangle$ as

$$\begin{aligned} |n\rangle &= \sum_j \alpha_j^s |v_j^s\rangle + \sum_j \alpha_j^a |v_j^a\rangle, \\ |N+1-n\rangle &= \sum_j \alpha_j^s |v_j^s\rangle - \sum_j \alpha_j^a |v_j^a\rangle. \end{aligned} \tag{3}$$

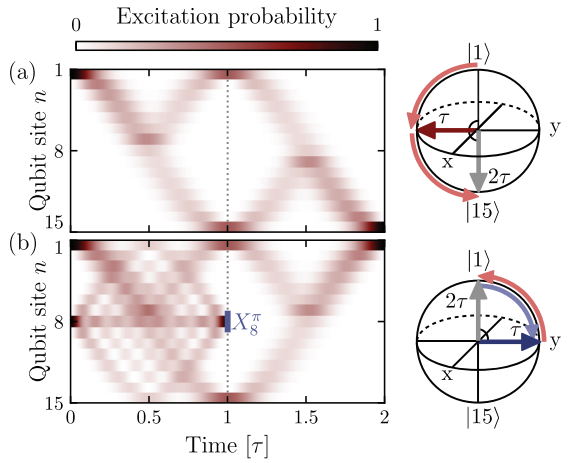

FIG. 2. Simulated occupation dynamics during two consecutive fractional state transfers (FST) on an $N=15$ qubit chain. Hamiltonian parameters are chosen to achieve a transfer angle $\theta = \pi/2$. (a) Evolution of an excitation prepared at site 1. After a first FST at time τ (dotted line), the chain is in a superposition of the excitation being at either of its ends. In the Bloch-sphere spanned by the states $|1\rangle$ and $|15\rangle$, this corresponds to a rotation by an angle $\pi/2$ (dark red arrow). At time 2τ after a second FST, the excitation refocuses at site 15, resulting in a $2\theta = \pi$ rotation on the Bloch-sphere (gray arrow). (b) Evolution of a state with excitations prepared at sites 1 and 8. In this case, the first FST rotates the state $|1\rangle$ on the Bloch-sphere by a negative angle $-\pi/2$ (dark blue arrow), due to the odd parity of excitations in the middle of the chain. In contrast, the center excitation refocuses at its original location and is then removed by an instantaneous π-flip gate X_8^π at site 8 (blue rectangle), which changes the parity. Then, with a second FST the dynamics are reverted and the excitation refocuses at site 1.

Specific transfer angles θ between mirror-symmetric states can be achieved by choosing the parameters J_n and Δ_n such that the eigenvalues of $H_N^{(1)}$ have the form

$$\lambda_j^{s/a}\tau = \pm\frac{\theta}{2} + \phi + m_j^{s/a} 2\pi, \tag{4}$$

with m_j^s, $m_j^a \in \mathbb{Z}$ and ϕ is a phase acquired during transfer (see Appendix A). Evolving the state $|n\rangle$ according to these eigenvalues and eigenstates for transfer time τ results in

$$\begin{aligned} e^{-iH_N^{(1)}\tau}|n\rangle &= \sum_j e^{-i\lambda_j^s\tau}\alpha_j^s|v_j^s\rangle + \sum_j e^{-i\lambda_j^a\tau}\alpha_j^a|v_j^a\rangle \\ &= e^{-i\phi}\left(\cos\left(\frac{\theta}{2}\right)|n\rangle - i\sin\left(\frac{\theta}{2}\right)|N+1-n\rangle\right). \end{aligned} \tag{5}$$

Thus, qubit n and its mirror qubit on the chain, qubit $N+1-n$, are rotated by an angle θ in their respective two-qubit subspace, which realizes FST. Using the software package QuTiP [52], we simulate the dynamics in the single-excitation manifold for a chain with length $N=15$ and parameters such that $\theta = \pi/2$ as shown in Fig. 2(a). After time τ, a system initially in $|1\rangle$ is rotated to the superposition state $(|1\rangle - i|15\rangle)/\sqrt{2}$. After time 2τ, the total transfer angle is $2\theta = \pi$ and the excitation refocuses in state $|15\rangle$.

III. PARITY-DEPENDENT COUPLINGS

We now consider the full unitary evolution under H_N for arbitrary initial states by using a mapping between one-dimensional spin chains and free fermions [39]. Thus, we extend previous results to find that FST with multiple excitations leads to parity-dependent couplings between mirror-symmetric qubit sites. Specifically, we provide an intuition for the resulting interactions between qubits by mapping the time evolution under H_N to the dynamics of an effective nonlocal Hamiltonian,

$$\begin{aligned} G_N = {} & \sigma_1^+ \otimes Z_2 \otimes Z_3 \otimes \cdots \otimes Z_{N-2} \otimes Z_{N-1} \otimes \sigma_N^- \\ & + I_1 \otimes \sigma_2^+ \otimes Z_3 \otimes \cdots \otimes Z_{N-2} \otimes \sigma_{N-1}^- \otimes I_N \\ & + \cdots + \text{H.c.} \end{aligned} \tag{6}$$

At integer multiples of the transfer time τ, the time evolution under H_N generates the same unitary, up to single-qubit phases, as the evolution under G_N for a transfer angle θ. Indeed, the unitary $K_N = \exp(-i\theta G_N/2)$ can be realized by FST through

$$\exp\left(-i\frac{\theta}{2}G_N\right) = \exp(-iH_N\tau)\exp(i\phi H_z), \tag{7}$$

where $H_z = \sum_n \sigma_n^+\sigma_n^-$ accounts for the phase difference by local unitary transformation and would include an additional phase $\theta/2$ for the middle qubit in odd chains.

The form of G_N explicitly shows the parity-dependent mirror-symmetric rotation of excitations along the chain. Therefore, at stroboscopic times, the evolution under H_N can be understood as a rotation between each pair of mirror qubits, where the sign of the rotation angle is given by the parity of all qubits between them (see Figs. 1 and 2). Since the different terms in the sum of Eq. (6) commute, these rotations are independent of each other.

To prove Eq. (7), we analyze the Hamiltonians H_N, G_N, and H_z in terms of fermionic operators using a Jordan-Wigner transformation (JWT) [12]. We find that all transformed Hamiltonians describe noninteracting fermions. Therefore, their complete dynamics can be constructed from the single-excitation manifold using Slater determinants [53]. Since the single-excitation dynamics of both sides of the equation are equivalent, this construction leads to the same unitary evolution, and therefore Eq. (7) holds in all excitation manifolds (see Appendix B).

To demonstrate the parity dependence, we simulate the time evolution under H_N in the full Hilbert space for two consecutive FST processes with $\theta = \pi/2$ and with a parity change between them. We prepare two excitations, one at the origin and one at the center of the chain. After evolving for time τ, the excitation from the origin of the chain is partially transferred to the other end of the chain, while the excitation in the middle of the chain refocuses at the same site. We then remove the center excitation with an instantaneous X gate, thus changing the parity in the center of the chain. Evolving for a further time τ, the rotation angle θ is now inverted, causing a reversal of the dynamics as shown in Fig. 2(b). Indeed, the initial excitation at site 1 returns to its original position, in contrast to the dynamics of Fig. 2(a), where the parity is identical for both FST processes.

IV. APPLICATIONS

A. Fermion simulation

Fermions can be simulated on a quantum computer by using the Jordan-Wigner transformation [54,55] with fermionic annihilation operators $a_n = -(\otimes_{k=1}^{n-1} Z_k) \otimes \sigma_n^-$. For one-dimensional fermionic systems, nearest-neighbor couplings are easily simulated on qubit systems with local two-qubit gates [56]. However, in two-dimensional systems or ladder-type geometries, nearest-neighbor couplings are challenging because the one-dimensional structure of the Jordan-Wigner encoding leads to nonlocal operators. The JWT of G_N, $G_N^{\text{F}} = a_1^\dagger a_N + a_2^\dagger a_{N-1} + \cdots + \text{H.c.}$, creates long-range couplings between distant fermion sites, which can be used to implement such nonlocal terms. For example, when folding an even chain in half, all rung couplings of the system are directly implemented by G_N, which enables efficient simulation of the fermionic dynamics. To assess the efficiency, we implement the evolution under G_N for arbitrary times by either applying FST with the correct rotation angle or by decomposing its action into consecutive two-qubit gates based on FSWAP-networks [55,57] (see Appendix C). The correction of single-qubit phases acquired during FST takes a negligible amount of time since it can be implemented by single-qubit gates executed in parallel. Assuming that the gate speed is limited by the maximal achievable coupling $J_{\max}$, we find that by applying FST we can achieve a speedup of at least a factor 2 for odd N and $\sqrt{3}$ for even $N > 4$, with greater improvements for shorter chain lengths (see Fig. 3). The nonlocal couplings of FST can, therefore, be used to implement fast Trotter simulations of fermionic systems.

B. Parity measurement

Due to their native parity-dependent property, FST gates can also be harnessed to quickly measure correlators on long qubit chains, with applications in error correction, e.g., in low-density parity-check codes [49]. To this end, consider a qubit chain in the state $|\psi_m\rangle$ with m excitations. Its parity can be measured by introducing an auxiliary qubit on each end of the chain. After applying the sequence of gates

$$\begin{aligned} & \left[X_{\text{L}}^{\frac{\pi}{2}} K_{N+2}^{(\pi)} Y_{\text{R}}^{\frac{\pi}{2}}\right] |0\rangle_{\text{L}} |\psi_m\rangle |0\rangle_{\text{R}} \\ & \quad = \begin{cases} -i|1\rangle_{\text{L}}|\bar{\psi}_m\rangle|0\rangle_{\text{R}} & \text{for } m \text{ even}, \\ |0\rangle_{\text{L}}|\bar{\psi}_m\rangle|0\rangle_{\text{R}} & \text{for } m \text{ odd}, \end{cases} \end{aligned} \tag{8}$$

a measurement of the left auxiliary reveals the parity of excitations in the qubit chain. Here, $|\bar{\psi}_m\rangle = K_N^{(\pi)}|\psi_m\rangle$, $X_{\text{L}}^{\frac{\pi}{2}}$ ($Y_{\text{R}}^{\frac{\pi}{2}}$) is a π-half X (Y) -rotation on the left (right) auxiliary, and $K_{N+2}^{(\pi)}$ is the FST gate on the extended chain including the auxiliary qubits with $\theta = \pi$. This protocol requires $t \approx \frac{N+2}{2}\tau_{\text{iSWAP}}$, where $\tau_{\text{iSWAP}} = \frac{\pi}{2J_{\max}}$ is the time required for a nearest-neighbor iSWAP gate [see Eq. (A4)]. In comparison, a protocol based on two-qubit gates would require at least N such gates. The operation on the middle part of the chain can be reversed by applying $K_N^{(\pi)}$, increasing the required time to $t \approx (N+1)\tau_{\text{iSWAP}}$. However, for applications that perform repeated parity measurements of the same chain, this reversion is unnecessary since $(K_N^{(\pi)})^2 = I$ up to single-qubit

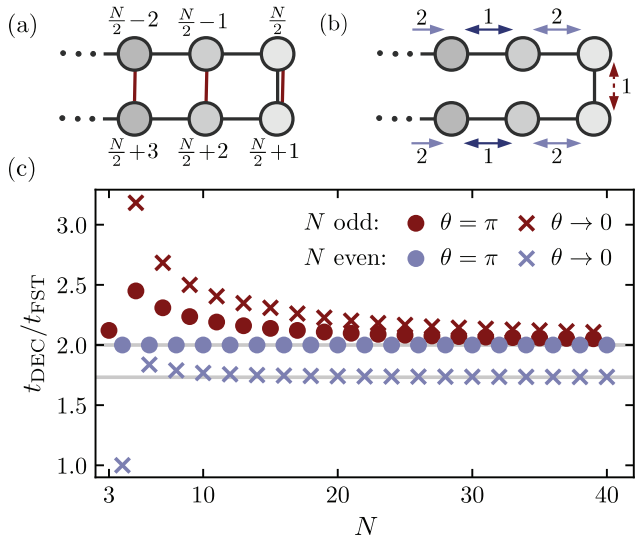

FIG. 3. Comparison between fractional state transfer (FST) and equivalent decomposition. (a) An even chain folded in the middle forms a ladder, where FST introduces effective interactions along its rungs corresponding to the different terms of G_N (red lines). (b) Decomposition of FST into two-qubit gates for even chains. Steps one (red and dark blue arrows) and two (light blue arrows) are repeated $N/2$ times. Blue arrows symbolize FSWAP gates, while the red arrow is an iSWAP(θ) gate. Odd chains are discussed in Appendix C. (c) Relative speed gain of FST with respect to the two-qubit gate decomposition of $\exp(-i\theta G_N/2)$ as a function of the chain length N for both odd (red) and even (blue) N. The speed of FST is assumed to be limited by the maximum coupling in the chain as given in Eq. (A1). For $N > 4$ and perfect state transfer, i.e., $\theta = \pi$, FST is at least a factor of 2 (upper solid line) faster. For $N > 4$ and transfer angles approaching zero, i.e., $\theta \to 0$, the same speedup is still present for N odd but reduces to $\sqrt{3}$ (lower solid line) for N even. $N = 3$ and 4 are special cases since some steps of the decomposition contain only iSWAP(θ) gates, which are faster for smaller θ. The point for $N = 3$ and $\theta \to 0$ is not shown since $t_{\mathrm{FST}} \to 0$ in this case.

Z-rotations. Furthermore, by applying single-qubit rotations before and after the measurement to introduce a basis change, any desired combination of correlators $P_1 P_2 \cdots P_N$ with $P \in \{X, Y, Z\}$ can be measured.

C. Three-qubit gate

Applying FST on a three-qubit chain leads to an interesting multiqubit gate, which directly implements a parametrizable fermionic next-nearest-neighbor interaction under JWT,

$$K_3 = |0\rangle\langle 0|_2 \otimes \mathrm{iSWAP}_{13}(-\theta) + |1\rangle\langle 1|_2 \otimes \mathrm{iSWAP}_{13}(\theta),$$

where the indices indicate the qubit positions. We assume that the gate speed is limited by the maximum coupling $J_{\max}$, since high detunings are usually experimentally feasible [58–60]. Given this assumption, the FST gate is significantly faster than its decomposition in two-qubit gates given by $\mathrm{FSWAP}_{12}\mathrm{iSWAP}_{23}(-\theta)\mathrm{FSWAP}_{12}$, where FSWAP is the fermionic swap gate [55] [Fig. 4(c)]. Since this speedup increases for smaller angles, the FST gate is well suited for variational quantum algorithms and Trotter simulations, which often require only short interaction steps [61].

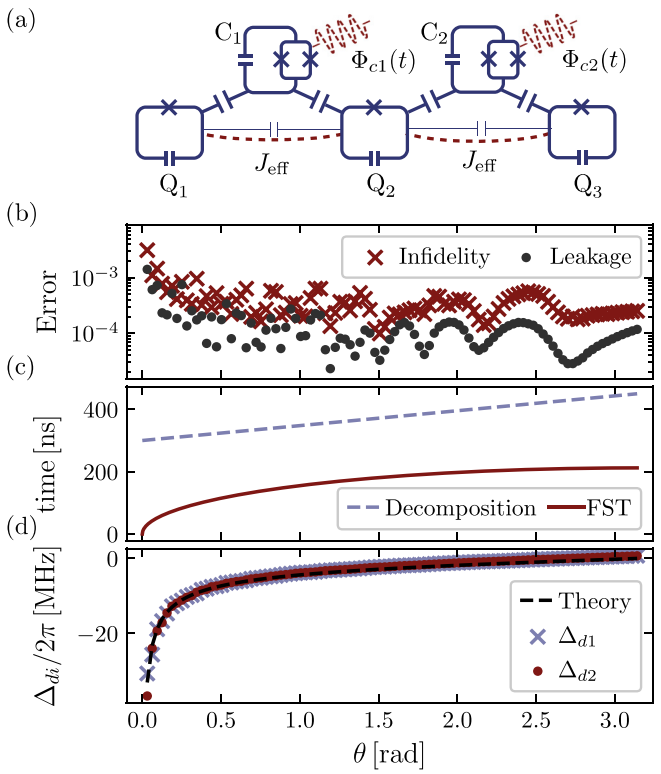

FIG. 4. Simulation of the three-qubit fractional-state-transfer gate for superconducting qubits. (a) Three fixed-frequency transmons (Q_1, Q_2, Q_3) are coupled via two tunable couplers (C_1, C_2). By periodically modulating the coupler frequencies through flux pulses (Φ_{c1}, Φ_{c2}), effective interactions between the qubits arise (J_{eff}). (b) Infidelity and leakage (population losses out of the computational subspace averaged over the computational states) of the optimized gate at various angles. (c) The total gate time for different θ is set as theoretically predicted (solid red). The gate time is significantly shorter than the decomposition into two-qubit gates (dashed blue). (d) Detuning of both drives (markers lie exactly over each other) and theoretical prediction (dashed line). The detuning is slightly shifted from the prediction because of ac-stark shifts.

V. SIMULATION

To assess the experimental feasibility of this three-qubit gate, we numerically simulate it in a superconducting architecture using the q-optimize software package [62]. The simulated setup contains three fixed-frequency transmons that are dispersively coupled with two flux-tunable coupler transmons as shown in Fig. 4(a). Each transmon is modeled as a nonlinear Duffing oscillator with three energy levels each described by the Hamiltonian stated in Eq. (D1) (see Appendix D) with the chosen Hamiltonian parameters summarized in Table I. Effective couplings between neighboring qubits are induced by periodically modulating the coupler frequency [63]. We adjust the flux drive amplitudes to change the strength of the effective coupling J and the frequency of the drives to modify the detuning Δ, to realize the effective Hamiltonian H_3 required for FST (see Appendix D). As the interactions are mediated by parametric drives, the gate is compatible with single-qubit virtual Z gates [64].

TABLE I. Hamiltonian parameters used in simulation.

Parameter	Value
$\omega_1/2\pi$	5.05 GHz
$\omega_2/2\pi$	5.00 GHz
$\omega_3/2\pi$	5.075 GHz
$\omega_{c1}/2\pi$ (at Φ_{c1}^{DC})	6.086 GHz
$\omega_{c2}/2\pi$ (at Φ_{c2}^{DC})	6.106 GHz
$\alpha_1/2\pi, \alpha_2/2\pi, \alpha_3/2\pi$	−300 MHz
$\alpha_{c1}/2\pi, \alpha_{c2}/2\pi$	−350 MHz
$\Phi_{c1}^{\mathrm{DC}}, \Phi_{c2}^{\mathrm{DC}}$	$0.3\Phi_0$
d_{c1}, d_{c2}	0.5
$g_{1,c1}/2\pi, g_{2,c2}/2\pi$	100 MHz
$g_{2,c1}/2\pi, g_{3,c2}/2\pi$	−100 MHz
$g_{1,2}/2\pi, g_{2,3}/2\pi$	−6.6 MHz

As our gate relies on states in the single and second-excitation manifold having the same energy level spacing, we position the couplers at frequencies in the dispersive regime where unwanted ZZ-type couplings vanish [65] while still having sufficient mediated coupling between the qubits of approximately $3.7 \times 2\pi$ MHz [see Eq. (D6)]. For the drive on coupler ci we use a flattop Gaussian envelope given by $A_{ci}(t) = \Phi_{ci}^{\mathrm{A}}[1 + \mathrm{erf}(t/\tau_{\mathrm{r}} - 2)][1 + \mathrm{erf}((\tau_{\mathrm{final}} - t)/\tau_{\mathrm{r}} - 2)]/4$, where erf is the Gauss error function, τ_{final} is the gate length, τ_{r} is the rise time of the pulse, and Φ_{ci}^{A} is the amplitude of the drive. We optimize these amplitudes only once at $\theta = \pi$ and keep $\Phi_{c1}^{\mathrm{A}} = 0.0534\Phi_0$, $\Phi_{c2}^{\mathrm{A}} = 0.0529\Phi_0$ fixed for all θ. Here Φ_0 denotes the magnetic flux quantum. The envelope is sampled with a finite resolution of 2.4 GHz to realistically model an arbitrary waveform generator and then mixed with a local oscillator signal.

We optimize the frequency of both gate pulses for a range of effective transfer angles $\theta \in [0.01\pi, \pi]$ assuming perfect single-qubit virtual Z gates [64]. The optimization uses the L-BFGS-B algorithm [66] with gradients calculated by numerical differentiation. For $\theta = \pi$, we use a gate time of $\tau_{\mathrm{final}} = 212$ ns and $\tau_{\mathrm{r}} = 2$ ns. For smaller angles, the pulse envelope is scaled following the theoretical prediction for constant coupling strength in Eq. (D14) [see the red curve in Fig. 4(c)].

We calculate the average infidelity [67] of the evolution operator obtained by numerically solving Schrödinger's equation. Without taking finite coherence into account, average infidelities lower than 10^{-3} are achieved for $\theta \in [0.1, \pi]$ [see Fig. 4(b)]. The fidelity is mainly limited by leakage to the second-excited states of the qubits, which oscillates periodically with the gate length. This leakage is caused by the off-resonantly driven transitions to the second-excited qubit states via higher harmonics of the drive. For $\theta \lesssim 0.1$, the infidelity and leakage increase because of sharp envelopes needed for the shorter gate durations, which become comparable to an oscillation period of the drive frequencies. In this regime, the assumption of an effective interaction between the qubits mediated through the periodic coupler modulation is not valid anymore. The drive detunings Δ_{di} closely follow the theoretical prediction with small deviations caused by ac-stark shifts induced by the drive [see Fig. 4(d)]. Since the detunings vary smoothly with θ, it is expected that, in an experiment, the gate could be optimized for only a few reference transfer angles and the detunings for other θ extracted by interpolation.

VI. CONCLUSION

We have demonstrated how simultaneous nearest-neighbor couplings between qubits on a chain can be harnessed to generate dynamics equivalent to complex nonlocal interactions. Building on FST, we have engineered long-range couplings dependent on qubit correlators along the chain. These directly implement fermionic coupling terms under a Jordan-Wigner transformation. The resulting multiqubit gates provide a significant speedup compared to an equivalent decomposition into two-qubit gates, making them promising candidates for the implementation of fermionic simulation or as a building block in quantum variational algorithms. Furthermore, we have shown that the parity-dependent property of FST gates can be harnessed for efficient measurements of qubit correlators, with applications in quantum error correction or quantum phase recognition [68].

We performed realistic numerical simulations of a superconducting-circuit three-qubit chain suggesting gate fidelities above 99.9% for a wide range of transfer angles under coherent evolution. The remaining infidelity is mostly caused by leakage and could be mitigated by pulse shaping [69,70] or engineering qubits with higher anharmonicities [71]. Moreover, the chosen protocol can readily be implemented with larger qubit numbers and embedded in a two-dimensional qubit architecture, since experimental pulse optimization has been realized successfully for up to 55 pulse parameters [70], and ZZ-type interactions between neighboring qubits can be suppressed [72].

In the next step, we can extend the current protocol by introducing time-dependent controls. Since qubit chains can be fully understood in the single-excitation manifold, even for large systems numerical simulations remain tractable. Therefore, optimal-control techniques can be used to explore the space of possible operations, thus enabling the discovery of a variety of high-fidelity multiqubit gates.

The presented data and the programs used for the simulations are available online [73].

ACKNOWLEDGMENTS

We thank Cosimo Rusconi, Ignacio Cirac, and Monika Aidelsburger for insightful discussions. F.R. acknowledges funding by the European Commission Marie Curie ETN project QuSCo (Grant No. 765267) and by GeCQoS (Grant No. 13N15680) project funded by the Federal Ministry of Education and Research (BMBF). C.S. has received funding from the European Union's Framework Programme for Research and Innovation Horizon 2020 (2014–2020) under the Marie Skłodowska-Curie Grant Agreement No. 754388 (LMUResearchFellows) and from LMUexcellent, funded by the BMBF and the Free State of Bavaria under the Excellence Strategy of the German Federal Government and the Länder. We also acknowledge funding by the Deutsche Forschungsgemeinschaft (DFG, German Research Foundation)—Project No. FI 2549/1-1.

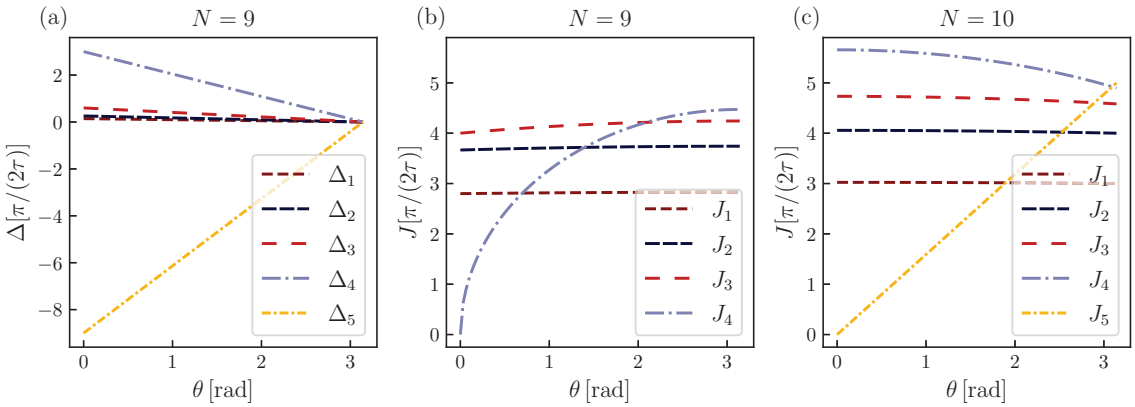

FIG. 5. Hamiltonian parameters J_n and Δ_n as a function of the transfer angle θ for chain length $N = 9$ in (a) and (b) and $N = 10$ in (c). (a) The magnitude of the required detunings decreases linearly with θ if N is odd. Perfect state transfer requires no detunings. For N even, no detunings are needed. (b) All coupling strengths increase with θ if N is odd. (c) For N even, only the center coupling increases with θ while all other couplings decrease.

APPENDIX A: HAMILTONIAN PARAMETERS FOR FST

Given its eigenvalues, a persymmetric tridiagonal matrix can be uniquely reconstructed. Taking the spectrum of $H_N^{(1)}$ to be as narrow as possible ($m_j^s = m_j^a$, $m_{j+1}^{s/a} = m_j^{s/a} + 1$) and the gate time to be τ, the required Hamiltonian parameters to achieve FST with a transfer angle of θ for a qubit chain with length N are [37,43]

$$J_n = \begin{cases} \frac{\pi}{2\tau}\sqrt{\frac{n(N-n)\left((N-2n)^2-\left(\frac{\theta}{\pi}\right)^2\right)}{(N-1-2n)(N+1-2n)}} & \text{for } N \text{ even}, \\ \frac{\pi}{2\tau}\sqrt{\frac{n(N-n)\left((N-2n)^2-\left(\frac{\theta}{\pi}-1\right)^2\right)}{(N-2n)^2}} & \text{for } N \text{ odd}, \end{cases} \tag{A1}$$

$$\Delta_n = \begin{cases} 0 \text{ for } N \text{ even}, \\ \frac{\pi}{2\tau}\frac{\left(\frac{\theta}{\pi}-1\right)N}{2}\left(\frac{1}{2n-N} - \frac{1}{2n-2-N}\right) & \text{for } N \text{ odd}. \end{cases} \tag{A2}$$

As the coupling strengths and detunings cannot be chosen arbitrarily large in experimental realizations, they determine the speed of our operation. For perfect state transfer, when $\theta = \pi$, the formulas simplify to the known result of

$$J_n = \frac{\pi}{2\tau}\sqrt{n(N-n)}, \tag{A3}$$

with $\Delta_n = 0$. Hence, the biggest required coupling is in the middle of the chain, where $J_{N/2} = \frac{\pi}{2\tau}\frac{N}{2}$ ($J_{(N+1)/2} = \frac{\pi}{4\tau}\sqrt{N^2-1}$) for N even (odd). Then, for a maximal coupling $J_{\max}$, perfect state transfer would be implemented in

$$\tau = \begin{cases} \frac{N\pi}{4J_{\max}} & \text{for } N \text{ even}, \\ \frac{\sqrt{N^2-1}\pi}{4J_{\max}} & \text{for } N \text{ odd}. \end{cases} \tag{A4}$$

For FST we analyze the behavior as we reduce the transfer angle θ from $\theta = \pi$ in the perfect state transfer case: for N odd we have $\frac{dJ_n}{d\theta} \geqslant 0$ indicating a speed-up for smaller angles; for N even $\frac{dJ_n}{d\theta} \leqslant 0\,\forall n \neq \frac{N}{2}$ and $\frac{dJ_n}{d\theta} \geqslant 0$ for $n = \frac{N}{2}$ resulting in increased gate times at small angles. In fact, the operation time is the longest for $\theta \to 0$ (see Fig. 5). Upper bounds for the minimum gate times τ holding for all θ are given, in terms of the highest coupling $J_{\max}$, as

$$\tau \leqslant \begin{cases} \frac{\pi}{2\sqrt{3}J_{\max}}\sqrt{N^2-4} & \text{for } N \text{ even}, \\ \frac{\pi}{4J_{\max}}\sqrt{N^2-1} & \text{for } N \text{ odd}. \end{cases} \tag{A5}$$

For N odd, the required range of detunings is

$$\Delta_{\max} - \Delta_{\min} = \frac{N(\pi-\theta)}{3\tau}. \tag{A6}$$

APPENDIX B: DETAILS ON THE MAPPING BETWEEN H_N AND G_N

The single-excitation manifold matrix elements of $U_N = \exp(-i\tau H_N)$ and $K_N = \exp(-i\frac{\theta}{2}G_N)$ are

$$\begin{aligned} \langle n|U_N|m\rangle &= e^{-i\phi}\left(\cos\left(\frac{\theta}{2}\right)\delta_{n,m} - i\sin(\frac{\theta}{2})\delta_{n,N+1-m}\right), \\ \langle n|K_N|m\rangle &= \cos\left(\frac{\theta}{2}\right)\delta_{n,m} - i\sin\left(\frac{\theta}{2}\right)\delta_{n,N+1-m}, \end{aligned} \tag{B1}$$

with the special case of the middle qubit when N is odd,

$$\begin{aligned} \left\langle \frac{N+1}{2}\middle|U_N\middle|\frac{N+1}{2}\right\rangle &= e^{-i(\phi+\theta/2)}, \\ \left\langle \frac{N+1}{2}\middle|K_N\middle|\frac{N+1}{2}\right\rangle &= 1. \end{aligned} \tag{B2}$$

These matrix elements can be aligned by the local unitary rotation $U_z = \exp(i\phi H_z)$, with

$$H_z = \begin{cases} \sum_n \sigma_n^+\sigma_n^- & \text{for } N \text{ even}, \\ \sum_n \sigma_n^+\sigma_n^- + \frac{\theta}{2\phi}\sigma_{\frac{N+1}{2}}^+\sigma_{\frac{N+1}{2}}^- & \text{for } N \text{ odd}, \end{cases} \tag{B3}$$

such that the equivalence $K_N = U_N U_z$ is shown to hold in the single-excitation manifold. To show this equivalence in all excitation manifolds, we use the Jordan-Wigner transformation with fermionic annihilation operators $a_n = -(\otimes_{k=1}^{n-1}Z_k)\otimes\sigma_n^-$. The Jordan-Wigner transformation of the Hamiltonians H_N,

G_N, and H_z is given by

$$H_N^{\mathrm{F}} = \sum_{n=1}^{N-1}(J_n a_n^\dagger a_{n+1} + \mathrm{H.c.}) + \sum_{n=1}^{N}\Delta_n a_n^\dagger a_n, \tag{B4}$$

$$\begin{aligned} G_N^{\mathrm{F}} = {} & a_1^\dagger \otimes I_2 \otimes I_3 \otimes \cdots \otimes I_{N-2} \otimes I_{N-1} \otimes a_N \\ & + I_1 \otimes a_2^\dagger \otimes I_3 \otimes \cdots \otimes I_{N-2} \otimes a_{N-1} \otimes I_N \\ & + \cdots + \mathrm{H.c.} \end{aligned} \tag{B5}$$

and

$$H_z^{\mathrm{F}} = \begin{cases} \sum_n a_n^\dagger a_n \text{ for } N \text{ even}, \\ \sum_n a_n^\dagger a_n + \frac{\theta}{2\phi} a^\dagger_{\frac{N+1}{2}} a_{\frac{N+1}{2}} \text{ for } N \text{ odd}. \end{cases} \tag{B6}$$

Since these operators are all quadratic in the fermionic creation and annihilation operators, they describe noninteracting fermions [39,47], and their dynamics are fully determined in the single excitation manifold [53]. Therefore, $K_N = U_N U_z$, i.e., Eq. (7) of the main text, holds in all excitation manifolds.

APPENDIX C: DECOMPOSITION OF THE FST GATE INTO TWO QUBIT GATES

The decomposition of the FST gate uses the two qubit gates

$$\mathrm{iSWAP}(\theta) = \begin{pmatrix} 1 & 0 & 0 & 0 \\ 0 & \cos(\theta) & i\sin(\theta) & 0 \\ 0 & i\sin(\theta) & \cos(\theta) & 0 \\ 0 & 0 & 0 & 1 \end{pmatrix},$$

$$\mathrm{FSWAP} = \begin{pmatrix} 1 & 0 & 0 & 0 \\ 0 & 0 & 1 & 0 \\ 0 & 1 & 0 & 0 \\ 0 & 0 & 0 & -1 \end{pmatrix}. \tag{C1}$$

With the use of fermionic swap (FSWAP) gates played in parallel, electronic Hamiltonians can be simulated in linear depth and connectivity [57]. The decomposition presented here relies on this concept but further takes the effective ladder connectivity of FST into account to achieve a faster decomposition.

For N even, the FST gate is decomposed similarly to [55] by $N/2$ applications of the unitaries $U_1^{\mathrm{e}}U_2^{\mathrm{e}}$ as defined in Fig. 6(a). Since for $N > 4$ both U_1^{e} and U_2^{e} include full FSWAP gates, the decomposition takes time $N\pi/(2J_{\max})$ independent of θ. Comparing with Appendix A, we see that the direct implementation is at least a factor of $\sqrt{3}$ faster than its decomposition. For $\theta = \pi$, the gate takes half the decomposition's time. The total amount of gates required is $(N^2/2 - N)$ FSWAP gates and $N/2$ iSWAP gates. Since the gate count grows quadratically in N, coherent errors are also expected to grow with $\exp(N^2)$.

For N odd, the gate can be decomposed in a single application of $U_{\mathrm{start}}^{\mathrm{o}}$ followed by $(N-1)/2$ applications of $U_1^{\mathrm{o}}U_2^{\mathrm{o}}$ and a final application of $U_{\mathrm{final}}^{\mathrm{o}}$ as defined in Fig. 6(b). For $N > 3$ the whole decomposition takes time $(N+1)\pi/(2J_{\max})$. This time is at least twice as long as the direct implementation assuming the gate speed is limited by $J_{\max}$ and not the available detuning range. The total amount of gates needed is $(N-1)^2/2$ FSWAPs and $(N-1)/2$ iSWAPs and also grows quadratically with N.

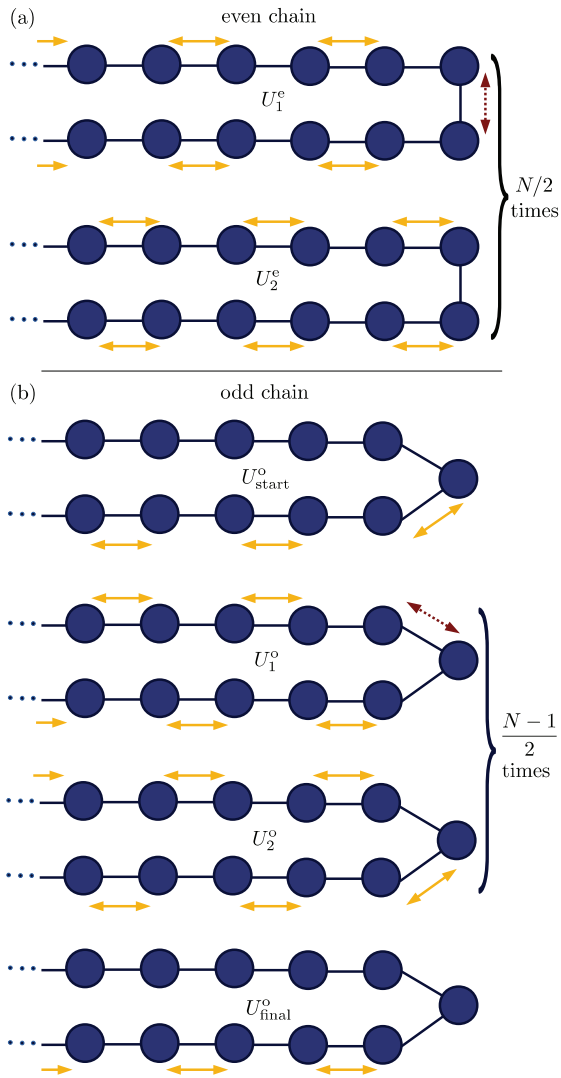

FIG. 6. Building blocks of the decomposition of the FST gate into two qubit gates. The chain is folded in half at the middle forming a ladder. Yellow arrows symbolize FSWAP gates. Red dotted arrows symbolize an iSWAP$(-\theta)$ gate. (a) For N even, the FST gate is decomposed by $N/2$ applications of $U_1^{\mathrm{e}}U_2^{\mathrm{e}}$. (b) For N odd, the FST gate is decomposed by a single application of $U_{\mathrm{start}}^{\mathrm{o}}$ followed by $(N-1)/2$ applications of $U_1^{\mathrm{o}}U_2^{\mathrm{o}}$ and a final application of $U_{\mathrm{final}}^{\mathrm{o}}$.

While we do not prove the optimality of these decompositions, there has been considerable effort to find efficient decompositions in the case of N even to enable Trotter simulation of a 2D-Fermi-Hubbard model [55]. To the authors' knowledge, no faster decomposition has been found so far.

APPENDIX D: EFFECTIVE HAMILTONIAN IN DRIVEN THREE-QUBIT CHAIN

The system Hamiltonian is given by

$$\begin{aligned} H = {} & \sum_{i\in 1,2,3}\left(\omega_i b_i^\dagger b_i + \frac{\alpha_i}{2} b_i^\dagger b_i^\dagger b_i b_i\right) \\ & + \sum_{i\in c1,c2}\left(\omega_i(\Phi_i) b_i^\dagger b_i + \frac{\alpha_i}{2} b_i^\dagger b_i^\dagger b_i b_i\right) \end{aligned}$$

$$
\begin{aligned}
&- \sum_{i\in 1,2} g_{i,c1}(b_i^\dagger - b_i)(b_{c1}^\dagger - b_{c1}) \\
&- \sum_{i\in 2,3} g_{i,c2}(b_i^\dagger - b_i)(b_{c2}^\dagger - b_{c2}) \\
&- g_{12}(b_1^\dagger - b_1)(b_2^\dagger - b_2) \\
&- g_{23}(b_2^\dagger - b_2)(b_3^\dagger - b_3),
\end{aligned} \tag{D1}
$$

with 1, 2, 3 ($c1$, $c2$) being the qubit (coupler) indices, b_i ($b_i^\dagger$) bosonic annihilation (creation) operators, ω_i (ω_{ci}) the bare frequencies of the qubits (couplers), α_i (α_{ci}) the anharmonicities of the qubits (couplers), $g_{i,cj}$ the coupling between qubit i and coupler j, and $|g_{i,j}| \ll |g_{i,cj}|$ the direct coupling between two neighboring qubits. The frequency ω_{ci} of coupler ci is modulated according to

$$
\omega_{ci}(\Phi_{ci}) = \alpha_{ci} + \left(\omega_{ci}^0 - \alpha_{ci}\right)\varphi(\Phi_{ci}), \tag{D2}
$$

where ω_{ci}^0 is the maximal coupler frequency,

$$
\varphi(\Phi_{ci}) = \sqrt[4]{\cos^2\left(\frac{\pi\Phi_{ci}}{\Phi_0}\right) + d_{ci}^2\sin^2\left(\frac{\pi\Phi_{ci}}{\Phi_0}\right)}, \tag{D3}
$$

Φ_{ci} is the applied flux, Φ_0 is the magnetic flux quantum, and $0 \leqslant d_{ci} \leqslant 1$ describes the asymmetry of the coupler. The couplers asymmetries d_{ci} and their flux bias-points Φ_{ci}^{DC} are chosen such that the average frequencies of the couplers do not shift substantially during the gate to still operate at the ZZ zero point.

If the couplers are in the dispersive regime ($|\frac{g_{i,cj}}{\omega_i - \omega_{cj}}| \ll 1$), they decouple from the dynamics, and the Hamiltonian can be simplified similarly to [74] by Schrieffer-Wolff transformation. We neglect terms of the order $|\frac{\alpha_i}{\omega_i - \omega_{cj}}| \approx 0.3$ in the Schrieffer-Wolff transformation since they only lead to shifted anharmonicities and terms describing ZZ-shifts [75], which do not contribute to the understanding of the effective interaction derived in the following. Finally, we obtain

$$
\begin{aligned}
H_{\mathrm{SWT}} = &\sum_{i\in 1,2,3}\left(\tilde{\omega}_i b_i^\dagger b_i + \frac{\alpha_i}{2} b_i^\dagger b_i^\dagger b_i b_i\right) \\
&+ \tilde{g}_{1,2}(b_1^\dagger b_2 + \mathrm{H.c.}) + \tilde{g}_{2,3}(b_2^\dagger b_3 + \mathrm{H.c.}),
\end{aligned} \tag{D4}
$$

where

$$
\begin{aligned}
\tilde{\omega}_1 &= \omega_1 - \frac{g_{1,c1}^2}{\Delta_{1,c1}} - \frac{g_{1,c1}^2}{\Sigma_{1,c1}}, \\
\tilde{\omega}_2 &= \omega_2 - \frac{g_{2,c1}^2}{\Delta_{2,c1}} - \frac{g_{2,c1}^2}{\Sigma_{2,c1}} - \frac{g_{2,c2}^2}{\Delta_{2,c2}} - \frac{g_{2,c2}^2}{\Sigma_{2,c2}}, \\
\tilde{\omega}_3 &= \omega_3 - \frac{g_{3c2}^2}{\Delta_{3,c2}} - \frac{g_{3,c2}^2}{\Sigma_{3,c2}},
\end{aligned} \tag{D5}
$$

and

$$
\begin{aligned}
\tilde{g}_{i,j}(\Phi) &= g_{i,j} - \frac{g_{i,ci}g_{j,ci}}{2}\sum_{n\in i,j}\left(\frac{1}{\Delta_{n,ci}(\Phi)} + \frac{1}{\Sigma_{n,ci}(\Phi)}\right), \\
\Delta_{n,ci}(\Phi) &= \omega_{ci}(\Phi) - \omega_n, \\
\Sigma_{n,ci}(\Phi) &= \omega_{ci}(\Phi) + \omega_n.
\end{aligned} \tag{D6}
$$

If we periodically drive the flux through the coupler i with amplitude A_{di} and frequency ω_{di}, we can expand $\tilde{g}_{i,j}(\Phi(t))$ in a Fourier series with coefficients $\bar{g}_{i,j}^{(n)}$:

$$
\tilde{g}_{i,j}(A_{di}\cos(\omega_{di}t)) = \sum_{n=-\infty}^{\infty}\bar{g}_{i,j}^{(n)}\exp(in\omega_{di}t). \tag{D7}
$$

Assuming $\omega_{d1} \approx |\tilde{\omega}_1 - \tilde{\omega}_2|$ and $\omega_{d2} \approx |\tilde{\omega}_2 - \tilde{\omega}_3|$, we can neglect higher sidebands and only consider $\bar{g}_{i,j}^{(1)}$. Restricting the Hamiltonian to two-level systems and going to a rotating frame with a unitary transformation given by

$$
\begin{aligned}
U = \exp(it\,[&(\tilde{\omega}_2 + \omega_{d1})\sigma_1^+\sigma_1^- + \tilde{\omega}_2\sigma_2^+\sigma_2^- \\
&+ (\tilde{\omega}_2 + \omega_{d2})\sigma_3^+\sigma_3^-]),
\end{aligned} \tag{D8}
$$

we end up with the effective Hamiltonian

$$
\begin{aligned}
H_{\mathrm{RF}} = &\Delta_{d1}\sigma_1^+\sigma_1^- + \Delta_{d2}\sigma_3^+\sigma_3^- + \bar{g}_{1,2}^{(1)}(\sigma_1^+\sigma_2^- + \mathrm{H.c.}) \\
&+ \bar{g}_{2,3}^{(1)}(\sigma_2^+\sigma_3^- + \mathrm{H.c.}),
\end{aligned} \tag{D9}
$$

where

$$
\begin{aligned}
\Delta_{d1} &= (\tilde{\omega}_1 - \tilde{\omega}_2) - \omega_{d1}, \\
\Delta_{d2} &= (\tilde{\omega}_3 - \tilde{\omega}_2) - \omega_{d2}.
\end{aligned} \tag{D10}
$$

By choosing $\Delta_{d1} = \Delta_{d2} = \Delta$ by adjusting the drive frequencies, setting $\bar{g}_{1,2}^{(1)} = \bar{g}_{2,3}^{(1)} = J$ by adjusting the flux drive amplitudes, and going into the frame rotating at frequency Δ, we get the effective Hamiltonian

$$
H_3 = -\Delta\sigma_2^+\sigma_2^- + J(\sigma_1^+\sigma_2^- + \sigma_2^+\sigma_3^- + \mathrm{H.c.}), \tag{D11}
$$

which is exactly the Hamiltonian needed for FST. The unitary

$$
K_3 = \exp\left(-i\theta(\sigma_1^+ Z_2\sigma_3^- + \mathrm{H.c.})\right) \tag{D12}
$$

is realized by setting

$$
\Delta = \frac{2J(\pi - \theta)}{\sqrt{(\pi - \frac{\theta}{2})\theta}}, \tag{D13}
$$

evolving under H_3 for

$$
\tau = \frac{\sqrt{(\pi - \frac{\theta}{2})\theta}}{J}, \tag{D14}
$$

and applying single-qubit Z-rotations. These parameters where also found in [26], where the middle qubit is replaced by a transmission line initially in the ground state and the other two qubits by resonators. The single-qubit Z-rotations needed are $U_{Z_{1/3}} = \exp(i\frac{\theta}{2}\sigma_{1/3}^+\sigma_{1/3}^-)$ and $U_{Z_2} = \exp(i\theta\sigma_2^+\sigma_2^-)$.

[1] Y. Kim, C. J. Wood, T. J. Yoder, S. T. Merkel, J. M. Gambetta, K. Temme, and A. Kandala, Scalable error mitigation for noisy quantum circuits produces competitive expectation values, arXiv:2108.09197.

[2] F. Arute, K. Arya, R. Babbush, D. Bacon, J. C. Bardin, R. Barends, S. Boixo, M. Broughton, B. B. Buckley, D. A. Buell *et al.*, Hartree-fock on a superconducting qubit quantum computer, Science **369**, 1084 (2020).

[3] Y. Nam, J.-S. Chen, N. C. Pisenti, K. Wright, C. Delaney, D. Maslov, K. R. Brown, S. Allen, J. M. Amini, J. Apisdorf *et al.*, Ground-state energy estimation of the water molecule on a trapped-ion quantum computer, npj Quantum Inf. **6**, 33 (2020).

[4] C. Hempel, C. Maier, J. Romero, J. McClean, T. Monz, H. Shen, P. Jurcevic, B. P. Lanyon, P. Love, R. Babbush, A. Aspuru-Guzik, R. Blatt, and C. F. Roos, Quantum Chemistry Calculations on a Trapped-Ion Quantum Simulator, Phys. Rev. X **8**, 031022 (2018).

[5] J. I. Cirac and P. Zoller, Goals and opportunities in quantum simulation, Nat. Phys. **8**, 264 (2012).

[6] K. Bharti, A. Cervera-Lierta, T. H. Kyaw, T. Haug, S. Alperin-Lea, A. Anand, M. Degroote, H. Heimonen, J. S. Kottmann, T. Menke, W.-K. Mok, S. Sim, L.-C. Kwek, and A. Aspuru-Guzik, Noisy intermediate-scale quantum algorithms, Rev. Mod. Phys. **94**, 015004 (2022).

[7] N. Moll, P. Barkoutsos, L. S. Bishop, J. M. Chow, A. Cross, D. J. Egger, S. Filipp, A. Fuhrer, J. M. Gambetta, M. Ganzhorn *et al.*, Quantum optimization using variational algorithms on near-term quantum devices, Quantum Sci. Technol. **3**, 030503 (2018).

[8] S. McArdle, S. Endo, A. Aspuru-Guzik, S. C. Benjamin, and X. Yuan, Quantum computational chemistry, Rev. Mod. Phys. **92**, 015003 (2020).

[9] T. Esslinger, Fermi-hubbard physics with atoms in an optical lattice, Annu. Rev. Condens. Matter Phys. **1**, 129 (2010).

[10] V. c. v. Havlíček, M. Troyer, and J. D. Whitfield, Operator locality in the quantum simulation of fermionic models, Phys. Rev. A **95**, 032332 (2017).

[11] S. B. Bravyi and A. Y. Kitaev, Fermionic quantum computation, Ann. Phys. **298**, 210 (2002).

[12] M. A. Nielsen, *The Fermionic Canonical Commutation Relations and the Jordan-Wigner Transform* (School of Physical Sciences, The University of Queensland, Queensland, Australia, 2005), Vol. 59.

[13] C. D. Bruzewicz, J. Chiaverini, R. McConnell, and J. M. Sage, Trapped-ion quantum computing: Progress and challenges, Appl. Phys. Rev. **6**, 021314 (2019).

[14] J. Clarke and F. K. Wilhelm, Superconducting quantum bits, Nature (London) **453**, 1031 (2008).

[15] P. Krantz, M. Kjaergaard, F. Yan, T. P. Orlando, S. Gustavsson, and W. D. Oliver, A quantum engineer's guide to superconducting qubits, Appl. Phys. Rev. **6**, 021318 (2019).

[16] C. Kloeffel and D. Loss, Prospects for spin-based quantum computing in quantum dots, Annu. Rev. Condens. Matter Phys. **4**, 51 (2013).

[17] L. Henriet, L. Beguin, A. Signoles, T. Lahaye, A. Browaeys, G.-O. Reymond, and C. Jurczak, Quantum computing with neutral atoms, Quantum **4**, 327 (2020).

[18] P. Kok, W. J. Munro, K. Nemoto, T. C. Ralph, J. P. Dowling, and G. J. Milburn, Linear optical quantum computing with photonic qubits, Rev. Mod. Phys. **79**, 135 (2007).

[19] N. M. Linke, D. Maslov, M. Roetteler, S. Debnath, C. Figgatt, K. A. Landsman, K. Wright, and C. Monroe, Experimental comparison of two quantum computing architectures, Proc. Natl. Acad. Sci. (USA) **114**, 3305 (2017).

[20] A. Cowtan, S. Dilkes, R. Duncan, A. Krajenbrink, W. Simmons, and S. Sivarajah, On the qubit routing problem, in *14th Conference on the Theory of Quantum Computation, Communication and Cryptography (TQC 2019)*, Leibniz International Proceedings in Informatics (LIPIcs) (Schloss Dagstuhl–Leibniz-Zentrum fuer Informatik, Wadern, Germany, 2019), Vol. 135, pp. 5:1–5:32.

[21] J. Kempe, A. Kitaev, and O. Regev, The complexity of the local hamiltonian problem, in *FSTTCS 2004: Foundations of Software Technology and Theoretical Computer Science* (Springer, Berlin, 2005), pp. 372–383.

[22] R. Babbush, B. O'Gorman, and A. Aspuru-Guzik, Resource efficient gadgets for compiling adiabatic quantum optimization problems, Ann. Phys. **525**, 877 (2013).

[23] K. Zhang, H. Li, P. Zhang, J. Yuan, J. Chen, W. Ren, Z. Wang, C. Song, D.-W. Wang, H. Wang *et al.*, Synthesizing Five-Body Interaction in a Superconducting Quantum Circuit, Phys. Rev. Lett. **128**, 190502 (2022).

[24] F. Kranzl, M. K. Joshi, C. Maier, T. Brydges, J. Franke, R. Blatt, and C. F. Roos, Controlling long ion strings for quantum simulation and precision measurements, Phys. Rev. A **105**, 052426 (2022).

[25] X. Gu, J. Fernández-Pendás, P. Vikstål, T. Abad, C. Warren, A. Bengtsson, G. Tancredi, V. Shumeiko, J. Bylander, G. Johansson, and A. F. Kockum, Fast multiqubit gates through simultaneous two-qubit gates, PRX Quantum **2**, 040348 (2021).

[26] L. D. Burkhart, J. D. Teoh, Y. Zhang, C. J. Axline, L. Frunzio, M. H. Devoret, L. Jiang, S. M. Girvin, and R. J. Schoelkopf, Error-detected state transfer and entanglement in a superconducting quantum network, PRX Quantum **2**, 030321 (2021).

[27] C. W. Warren, J. Fernández-Pendás, S. Ahmed, T. Abad, A. Bengtsson, J. Biznárová, K. Debnath, X. Gu, C. Križan, A. Osman *et al.*, Extensive characterization of a family of efficient three-qubit gates at the coherence limit, arXiv:2207.02938.

[28] N. Glaser, F. Roy, and S. Filipp, Controlled-controlled-phase gates for superconducting qubits mediated by a shared tunable coupler, arXiv:2206.12392.

[29] M. Christandl, N. Datta, A. Ekert, and A. J. Landahl, Perfect State Transfer in Quantum Spin Networks, Phys. Rev. Lett. **92**, 187902 (2004).

[30] M.-H. Yung, Quantum speed limit for perfect state transfer in one dimension, Phys. Rev. A **74**, 030303(R) (2006).

[31] L. Vinet and A. Zhedanov, How to construct spin chains with perfect state transfer, Phys. Rev. A **85**, 012323 (2012).

[32] R. J. Chapman, M. Santandrea, Z. Huang, G. Corrielli, A. Crespi, M.-H. Yung, R. Osellame, and A. Peruzzo, Experimental perfect state transfer of an entangled photonic qubit, Nat. Commun. **7**, 11339 (2016).

[33] T. Brougham, G. M. Nikolopoulos, and I. Jex, Perfect transfer of multiple excitations in quantum networks, Phys. Rev. A **83**, 022323 (2011).

[34] G. M. Nikolopoulos, D. Petrosyan, and P. Lambropoulos, Electron wavepacket propagation in a chain of coupled quantum dots, J. Phys.: Condens. Matter **16**, 4991 (2004).

[35] T. Shi, Y. Li, Z. Song, and C.-P. Sun, Quantum-state transfer via the ferromagnetic chain in a spatially modulated field, Phys. Rev. A **71**, 032309 (2005).

[36] C. Albanese, M. Christandl, N. Datta, and A. Ekert, Mirror Inversion of Quantum States in Linear Registers, Phys. Rev. Lett. **93**, 230502 (2004).

[37] L. Vinet and A. Zhedanov, Para-krawtchouk polynomials on a bi-lattice and a quantum spin chain with perfect state transfer, J. Phys. A **45**, 265304 (2012).

[38] M.-H. Yung and S. Bose, Perfect state transfer, effective gates, and entanglement generation in engineered bosonic and fermionic networks, Phys. Rev. A **71**, 032310 (2005).

[39] A. Kay, Perfect, efficient, state transfer and its application as a constructive tool, Int. J. Quantum Inform. **08**, 641 (2010).

[40] X. Li, Y. Ma, J. Han, T. Chen, Y. Xu, W. Cai, H. Wang, Y. P. Song, Z.-Y. Xue, Z. Q. Yin, and L. Sun, Perfect Quantum State Transfer in a Superconducting Qubit Chain with Parametrically Tunable Couplings, Phys. Rev. Applied **10**, 054009 (2018).

[41] M. A. Nielsen and I. L. Chuang, *Quantum Computation and Quantum Information: 10th Anniversary Edition* (Cambridge University Press, Cambridge, 2010).

[42] M. H. Yung, D. Leung, and S. Bose, An exact effective two-qubit gate in a chain of three spins, Quantum Inf. Comput. **4**, 174 (2004).

[43] V. X. Genest, L. Vinet, and A. Zhedanov, Quantum spin chains with fractional revival, Ann. Phys. **371**, 348 (2016).

[44] A. Chan, G. Coutinho, C. Tamon, L. Vinet, and H. Zhan, Quantum fractional revival on graphs, Discrete Appl. Math. **269**, 86 (2019).

[45] J.-M. Lemay, L. Vinet, and A. Zhedanov, An analytic spin chain model with fractional revival, J. Phys. A **49**, 335302 (2016).

[46] L. G. Valiant, Quantum circuits that can be simulated classically in polynomial time, SIAM J. Comput. **31**, 1229 (2002).

[47] B. M. Terhal and D. P. DiVincenzo, Classical simulation of noninteracting-fermion quantum circuits, Phys. Rev. A **65**, 032325 (2002).

[48] E. Knill, Fermionic linear optics and matchgates, arXiv:quant-ph/0108033.

[49] L. Z. Cohen, I. H. Kim, S. D. Bartlett, and B. J. Brown, Low-overhead fault-tolerant quantum computing using long-range connectivity, Sci. Adv. **8**, eabn1717 (2022).

[50] D. Lidar and T. Brun, *Quantum Error Correction* (Cambridge University Press, Cambridge, 2013).

[51] H. Hochstadt, On some inverse problems in matrix theory, Arch. Math. **18**, 201 (1967).

[52] J. Johansson, P. Nation, and F. Nori, Qutip: An open-source python framework for the dynamics of open quantum systems, Comput. Phys. Commun. **183**, 1760 (2012).

[53] P. Cappellaro, L. Viola, and C. Ramanathan, Coherent-state transfer via highly mixed quantum spin chains, Phys. Rev. A **83**, 032304 (2011).

[54] G. Ortiz, J. E. Gubernatis, E. Knill, and R. Laflamme, Quantum algorithms for fermionic simulations, Phys. Rev. A **64**, 022319 (2001).

[55] C. Cade, L. Mineh, A. Montanaro, and S. Stanisic, Strategies for solving the Fermi-Hubbard model on near-term quantum computers, Phys. Rev. B **102**, 235122 (2020).

[56] E. Lieb, T. Schultz, and D. Mattis, Two soluble models of an antiferromagnetic chain, Ann. Phys. **16**, 407 (1961).

[57] I. D. Kivlichan, J. McClean, N. Wiebe, C. Gidney, A. Aspuru-Guzik, G. K.-L. Chan, and R. Babbush, Quantum Simulation of Electronic Structure with Linear Depth and Connectivity, Phys. Rev. Lett. **120**, 110501 (2018).

[58] F. Borjans, X. Croot, X. Mi, M. Gullans, and J. Petta, Resonant microwave-mediated interactions between distant electron spins, Nature (London) **577**, 195 (2020).

[59] J. Koch, T. M. Yu, J. Gambetta, A. A. Houck, D. I. Schuster, J. Majer, A. Blais, M. H. Devoret, S. M. Girvin, and R. J. Schoelkopf, Charge-insensitive qubit design derived from the cooper pair box, Phys. Rev. A **76**, 042319 (2007).

[60] M. D. Hutchings, J. B. Hertzberg, Y. Liu, N. T. Bronn, G. A. Keefe, M. Brink, J. M. Chow, and B. L. T. Plourde, Tunable Superconducting Qubits with Flux-Independent Coherence, Phys. Rev. Applied **8**, 044003 (2017).

[61] J. R. McClean, J. Romero, R. Babbush, and A. Aspuru-Guzik, The theory of variational hybrid quantum-classical algorithms, New J. Phys. **18**, 023023 (2016).

[62] N. Wittler, F. Roy, K. Pack, M. Werninghaus, A. S. Roy, D. J. Egger, S. Filipp, F. K. Wilhelm, and S. Machnes, Integrated Tool Set for Control, Calibration, and Characterization of Quantum Devices Applied to Superconducting Qubits, Phys. Rev. Applied **15**, 034080 (2021).

[63] D. C. McKay, S. Filipp, A. Mezzacapo, E. Magesan, J. M. Chow, and J. M. Gambetta, Universal Gate for Fixed-Frequency Qubits Via a Tunable Bus, Phys. Rev. Applied **6**, 064007 (2016).

[64] D. C. McKay, C. J. Wood, S. Sheldon, J. M. Chow, and J. M. Gambetta, Efficient Z gates for quantum computing, Phys. Rev. A **96**, 022330 (2017).

[65] E. A. Sete, A. Q. Chen, R. Manenti, S. Kulshreshtha, and S. Poletto, Floating Tunable Coupler for Scalable Quantum Computing Architectures, Phys. Rev. Applied **15**, 064063 (2021).

[66] C. Zhu, R. H. Byrd, P. Lu, and J. Nocedal, Algorithm 778: L-BFGS-B: Fortran subroutines for large-scale bound-constrained optimization, ACM Trans. Math. Softw. **23**, 550 (1997).

[67] M. A. Nielsen, A simple formula for the average gate fidelity of a quantum dynamical operation, Phys. Lett. A **303**, 249 (2002).

[68] J. Herrmann, S. M. Llima, A. Remm, P. Zapletal, N. A. McMahon, C. Scarato, F. Swiadek, C. K. Andersen, C. Hellings, S. Krinner *et al.*, Realizing quantum convolutional neural networks on a superconducting quantum processor to recognize quantum phases, arXiv:2109.05909.

[69] F. Motzoi, J. M. Gambetta, P. Rebentrost, and F. K. Wilhelm, Simple Pulses for Elimination of Leakage in Weakly Nonlinear Qubits, Phys. Rev. Lett. **103**, 110501 (2009).

[70] M. Werninghaus, D. J. Egger, F. Roy, S. Machnes, F. K. Wilhelm, and S. Filipp, Leakage reduction in fast superconducting qubit gates via optimal control, npj Quantum Inf. **7**, 14 (2021).

[71] F. Yan, Y. Sung, P. Krantz, A. Kamal, D. K. Kim, J. L. Yoder, T. P. Orlando, S. Gustavsson, and W. D. Oliver, Engineering framework for optimizing superconducting qubit designs, arXiv:2006.04130.

[72] J. Stehlik, D. M. Zajac, D. L. Underwood, T. Phung, J. Blair, S. Carnevale, D. Klaus, G. A. Keefe, A. Carniol, M. Kumph, M. Steffen, and O. E. Dial, Tunable Coupling Architecture for Fixed-Frequency Transmon Superconducting Qubits, Phys. Rev. Lett. **127**, 080505 (2021).

[73] M. Nägele, Programs used for the simulations and resulting data presented in this manuscript, https://github.com/MaxNaeg/Effective_non-local_parity-dependent_couplings_in_qubit_chains_code (2022).

[74] E. A. Sete, N. Didier, A. Q. Chen, S. Kulshreshtha, R. Manenti, and S. Poletto, Parametric-Resonance Entangling Gates with a Tunable Coupler, Phys. Rev. Applied **16**, 024050 (2021).

[75] L. Jin, Implementing high-fidelity two-qubit gates in superconducting coupler architecture with novel parameter regions, arXiv:2105.13306.